

FRONT MATTER

Title

- Satellite tidal magnetic signals constrain oceanic lithosphere-asthenosphere boundary
- Earth tomography with tidal magnetic signals

Authors

Alexander V. Grayver,^{1*} Neesha R. Schnepf², Alexey V. Kuvshinov¹, Terence J. Sabaka³, Chandrasekharan Manoj⁴ and Nils Olsen⁵

Affiliations

¹Institute of Geophysics, ETH Zürich, Sonneggstrasse 5, Zürich, Switzerland.

²Department of Geological Sciences/CIRES, University of Colorado, USA.

³Planetary Geodynamics Laboratory, NASA/GSFC, USA.

⁴NOAA's National Centers of Environmental Information/CIRES, University of Colorado, USA.

⁵DTU Space, Denmark.

* Corresponding author; e-mail: agrayver@erdw.ethz.ch; Tel.: +41 44 633 31 54

Abstract

The tidal flow of electrically conductive oceans through the geomagnetic field results in the generation of secondary magnetic signals, which provide information on the subsurface structure. Data from the new generation of satellites were shown to contain magnetic signals due to tidal flow; however, there are no reports that these signals have been used to infer subsurface structure. Here we use satellite-detected tidal magnetic fields to image the global electrical structure of the oceanic lithosphere and upper mantle down to a depth of about 250 km. The model derived from more than 12 years of satellite data reveals a ≈ 72 km thick upper resistive layer followed by a sharp increase in electrical conductivity likely associated with the lithosphere-asthenosphere boundary, which separates colder rigid oceanic plates from the ductile and hotter asthenosphere.

Short summary

Results on the oceanic upper mantle electrical structure revealed by the satellite-detected tidal magnetic signals are presented.

MAIN TEXT

Introduction

Electrical conductivity (the reciprocal of resistivity) provides a wealth of information on the thermal and compositional state of the Earth's mantle (1,2), with high sensitivity to small fractions of conductive phases such as fluids and partial melts. Conventionally, the electrical structure of the oceanic lithosphere and upper mantle has been studied with

seafloor magnetotelluric sounding using natural ionospheric excitation sources (3–5). Recent progress in the quality of satellite data as well as processing and modeling techniques now allows us to use another natural source: ocean tidal flow. Secondary electromagnetic fields produced by the electrically conductive seawater flowing through the ambient geomagnetic field obey Maxwell's equations:

$$\mu^{-1} \nabla \times \vec{B} = \sigma \vec{E} + \vec{j}^{ext} \quad (1)$$

$$\nabla \times \vec{E} = i\omega \vec{B},$$

where \vec{E}, \vec{B} respectively are electric and magnetic fields, μ, σ are magnetic permeability and electrical conductivity of the medium, ω is the angular frequency and \vec{j}^{ext} is the extraneous current due to tidal flow given by

$$\vec{j}^{ext} = \sigma_s (\vec{v} \times \vec{B}^{main}). \quad (2)$$

Here, σ_s is the conductivity of seawater (Figure 1d), \vec{B}^{main} is the Earth's main (core) magnetic field (Figures 1a-c), $\vec{v} = \vec{u} / h$, h is the height of the water column and \vec{u} is the depth-integrated seawater velocity due to tidal forces (Figure 1e,f) – a parameter that is well constrained by modern high-resolution assimilated global models of deep ocean tides (6, 7). In contrast to previous synthetic studies (8–10), all quantities - including σ_s - in equation (2) vary laterally. The phenomenon described by eqs. (1-2) is known as “motional induction” (11,12).

It was shown that satellite data contain measurable magnetic signals due to tidal flow (8,9) and these signals possess sensitivity to subsurface structures (13). Attempts have been made to estimate bulk electrical properties of the subsurface using motionally induced electromagnetic signals recorded at isolated locations on land and the seafloor (14,15). These signals have also been used in ocean circulation studies (16), but their use for sounding Earth's conductivity was not reported to date.

Earth sounding with satellite-detected tidal magnetic signals differs from conventional electromagnetic (EM) sounding in several ways. Conventional methods, such as magnetotellurics, rely on a broad frequency content of the detected natural EM variations, whereas the tidal signal is limited to the frequency of the corresponding tide. By analogy with techniques such as Electrical Impedance Tomography (17), the sounding is still possible due to the spatially heterogeneous nature of the extraneous currents generated in the oceans and because induced secondary magnetic fields can be detected at multiple locations (for instance, at satellites). Another distinguishing feature is the galvanic coupling of the oceans with the seafloor. Methods with a purely inductive excitation mechanism (based on EM variations in the ionosphere or magnetosphere) are, generally, weakly influenced by the toroidal part of the exciting field. This leads to reduced sensitivity for resistive structures in the subsurface (18). In contrast, detected tidal magnetic signals (14) include this component through galvanic coupling and interaction of the induced fields with lateral inhomogeneities.

Results

The availability of more than 12 years of satellite and magnetic observatory data (19) enabled us to reliably extract the magnetic field due to the principal lunar semi-diurnal (M_2) tidal constituent (Figure 2a) as a dataset with unprecedented globally uniform spatial coverage. At a satellite altitude of 430 km, the tidal field has a maximum amplitude of 2.1 nT, which is a relatively weak signal compared to the maximum total magnetic field intensity at that height (up to 54,000 nT). Nevertheless, observed tidal magnetic signals cannot be explained with an insulating or uniform lithosphere and mantle (Figure 3a,b),

suggesting more information about Earth's interior structure is contained in these signals. We inverted the observed magnetic field due to tidal flow to obtain a global radially-variable conductivity model. The estimated model explains the observations remarkably well (Figure 2b; see also supplementary animation M1). Since motional induction occurs in the oceans, we observe weaker signals over continents. However, the field above the continents is not strictly zero because the observations occur at satellite altitude causing a portion of the signal to spread laterally.

Figure 4a illustrates the two best fit radially-varying conductivity models, as well as the conductivity of dry and water-saturated olivine (*I*) between depths of 80 and 400 km. We obtained the two models using different model constraints in the inversion algorithm. In the first case, smooth models were derived by minimizing differences between conductivities of the subsequent layers, whereas the second case results in structurally sparse models, by permitting sharp jumps in conductivity, but allowing as few features as possible. Both models explain the satellite observations almost equally well. The grey lines denote models whose misfit differs from the best fit models by $\leq 10\%$. Considering the model uncertainty, the dry and water-saturated olivine curves bracket the structurally sparse model within the entire depth range. However, the smooth model has lower conductivity in the range of 100-150 km. Another prominent difference between the models is the conductivity jump observed at a depth of 72 km in the structurally sparse model. Low misfit models indicate that the data fit varies insignificantly if the depth of this jump changes within 10-15 km. This jump can be associated with the lithosphere-asthenosphere boundary (LAB). Indeed, multiple seismic studies concluded that the average oceanic LAB depth occurs in the range of 70-80 km depth (20,21). Above the LAB, the colder rigid lithosphere is more resistive, whereas the asthenosphere is significantly more conductive due to its higher temperatures, as well as enhancements due to other mechanisms such as partial melt and water (3,5). Since the smooth model must respect the imposed smoothing constraints, it does not exhibit any jump at these depths. Assuming that the structurally sparse model represents a plausible scenario, the enhanced conductivity of the asthenosphere suggests abundance of partial melts and water in the upper mantle.

Figure 4b compares our resulting models with a range of local models obtained via seafloor magnetotelluric (MT) sounding for different geological settings (4,22), relying on natural electromagnetic variations originating in the ionosphere. This is a completely different and independent type of excitation than the motional induction due to tides used in this study. All MT models show conductive material concentrated immediately below the seafloor, corresponding to the water-saturated floor sediments, which affect obtained models at greater depths due to smoothing regularization used. Our models do not have this feature because we incorporated sediments a priori (see section Materials and Methods). Depending on the age of the underlying plate, the MT models show variable lithosphere thickness and increased conductivity below the LAB. At a depth of 250 km, all models are practically the same given model uncertainty at these depths (4). Note that the rather homogeneous character of our models below 250 km depth is likely associated with the low sensitivity of the tidal data to regions beyond these depths and should be interpreted with caution.

Several factors contribute to the uncertainty of the obtained models. Among them is the noise in the observed signal and error in the extraneous current defined by equation 2. The latter is calculated using the World Magnetic Model (23), HAMTIDE ocean tidal model (7) and laterally variable ocean electrical conductivity derived from ocean salinity and temperature data given by the World Ocean Atlas 2009. Uncertainty in these models will propagate to the modeled magnetic fields and can affect upper mantle conductivity models. To ensure reliability of the models, variance in the modeled magnetic field signals due to

uncertainty in the source need to be below noise level in the data. Little quantitative information is available about uncertainty of the aforementioned models making a rigorous error propagation analysis difficult to implement. Instead, we performed a series of sensitivity tests considering key factors for each of the quantities in the equation 2. We compared tidal magnetic signals modeled using HAMTIDE and TPX08-atlas – two independent and widely used data-assimilated tidal models. Although these models are independent, they use many similar data to estimate tidal flow, thus possibility of some peculiar systematic shift cannot be fully ruled out. On the other hand, since data-assimilated tidal models lack uncertainty information on the estimated tidal flow (24), this seems to be a reasonable way to get a proxy for their error. Figure 5a shows the absolute difference between radial magnetic field components calculated using both tidal models.

The differences are below the current noise level in the observed data. The effect of laterally variable ocean conductivity (LVOC) is more significant as can be seen in Figure 5b, showing absolute difference between radial magnetic field components calculated using constant ocean conductivity of 3.2 S/m and LVOC derived in this study (Figure 1d), justifying the usage of LVOC for inversion. LVOC is based on World Ocean Atlas data and equation of state (25), both leading to uncertainty in the LVOC. World Ocean Atlas does not provide uncertainty on its data, making it hard to estimate LVOC uncertainty. To overcome this, we assume that LVOC uncertainty is on the order of seasonal variations in LVOC, which can reach 0.2 S/m. Figure 5c shows the absolute difference in responses calculated for the annual average LVOC (Figure 1d) and the northern hemisphere winter LVOC. The difference is below 0.02 nT making this factor negligible. Finally, uncertainty in the main magnetic field \vec{B}^{main} may also play a role. The global uncertainty for the WMM is estimated to be ≈ 150 nT, largely coming from omission of other field components such as those due to lithosphere and ionosphere (23). Compared to the total field intensity, this error appears very small. Figure 5d shows the absolute difference between the modeled response with the extraneous current incorporating a lithosphere field that can reach few hundreds of nanotesla in the oceans. As anticipated, the difference is negligible, allowing us to model tidal magnetic signals with high accuracy.

Discussion and Conclusions

We demonstrated that tidal magnetic signals detected by satellites can be used to retrieve information on the electrical structure of the upper mantle. Initial residual fields were substantially reduced and the derived model explains the data well (Figure 3). With data uncertainty of 0.15 nT, the presented models have a normalized root-mean-square error of 1.05. The residuals between the extracted and modeled fields are zero-mean normally distributed, confirming that the derived model produces unbiased responses.

Our models provide the basis for a new constraint on upper mantle structure and can assist in mantle composition studies, which currently rely on seismic data and a limited number of regional electric models predominantly from the Pacific Ocean (26,27). One should consider, though, that the amplitude of the tidal magnetic signal and, hence, the amount of information about the subsurface that can be extracted from it, vary laterally (Figure 2). Therefore, derived models are more sensitive to the upper mantle structure in regions where signals are large. In addition, an average model tries to fit data globally and the presented estimate of a LAB depth does not incorporate observed variations in the lithosphere thickness (28), be it due to cooling, presence of partial melt, etc. Whether tidal magnetic signals can be used to map lateral variations in the upper mantle conductivity remains an open question and depends on the continued collection of high-quality satellite data (29).

The new approach presented here also offers a complement to the global deep sounding method which lacks sensitivity to the upper mantle's resistive structures (30,31). The improved conductivity model can also be used for more accurate modeling of the ocean circulation magnetic signals (16). The strong tidal forces on moons with subsurface liquid oceans (such as Europa and Ganymede) (32), as well as the significant ambient magnetic fields around them (33) facilitates motional induction (34) and, provided that sufficiently long and accurate magnetic field measurements will be available, the detected tidal magnetic signals may become useful in constraining their inner structure.

Materials and Methods

Data preparation

The extracted tidal magnetic signal was determined using a comprehensive inversion approach where multiple components of the geomagnetic field (such as the core, crust, etc.) are co-estimated (19). This obtained tidal field is compared with model values which depend on the extraneous current in the oceans, on ocean conductivity (provided as supplementary Dataset 1) and on the conductivity of the lithosphere and mantle.

The conductivity model was parameterized using a thin layer with spatial resolution of $2^\circ \times 2^\circ$ and 23 underlying homogeneous spherical layers of variable thickness (Figure 6). A fixed surface conductance map that incorporates the conductivity of the continents, oceans and seafloor sediments was used to account for the near-surface heterogeneous layer (as is shown in (10)).

Inversion

A non-linear regularized inversion method based on a global stochastic optimization algorithm was employed (35) to convert the radial magnetic field component due to the M_2 tidal flow into a radial electrical conductivity model of the oceanic lithosphere and upper mantle. This was done by minimizing the misfit between the observed and modelled radial magnetic fields. Modeling of the electromagnetic fields was performed using the three-dimensional integral equation approach (10). Our detailed work-flow is shown in Figure 6.

To estimate the low misfit models shown in Figure 4a, we sampled 1000 models for which misfit does not differ by more than 10% from best fit model misfit. This gives us a proxy for the uncertainty of the model. To perform this sampling, a two step procedure was adopted. First, we found the most probable model and identify low-misfit regions of the model space. This was done by using the stochastic optimization algorithm called the Covariance Matrix Adaptation Evolution Strategy (36). Using information obtained from the previous step, we drew samples from the equivalence domain by means of random sampling. In this case, equivalence domain is defined as a set of models for which the misfit is not significantly different from the best model misfit and that still follow constraints imposed by the regularization (35).

References and Notes

1. T. Katsura and T. Yoshino, Heterogeneity of Electrical Conductivity in the Oceanic Upper Mantle. in *The Earth's Heterogeneous Mantle*, 173–204, Springer International Publishing, 2015.
2. A. Khan, On earth's mantle constitution and structure from joint analysis of geophysical and laboratory-based data: An example. *Surveys in Geophysics*, vol. 37, no. 1, 149–189, 2016.

3. R. L. Evans, G. Hirth, K. Baba, D. Forsyth, A. Chave, and R. Mackie, Geophysical evidence from the MELT area for compositional controls on oceanic plates. *Nature*, vol. 437, no. 7056, 249–252, 2005.
4. K. Baba, H. Utada, T. nori Goto, T. Kasaya, H. Shimizu, and N. Tada, Electrical conductivity imaging of the Philippine Sea upper mantle using seafloor magnetotelluric data. *Physics of the Earth and Planetary Interiors*, vol. 183, no. 12, 44 – 62, 2010. Special Issue on Deep Slab and Mantle Dynamics.
5. S. Naif, K. Key, S. Constable, and R. Evans, Melt-rich channel observed at the lithosphere-asthenosphere boundary. *Nature*, vol. 495, no. 7441, 356–359, 2013.
6. G. D. Egbert and S. Y. Erofeeva, Efficient inverse modeling of barotropic ocean tides. *Journal of Atmospheric and Oceanic Technology*, vol. 19, no. 2, 183–204, 2002.
7. E. Taguchi, D. Stammer, and W. Zahel, Inferring deep ocean tidal energy dissipation from the global high-resolution data-assimilative HAMTIDE model. *Journal of Geophysical Research: Oceans*, vol. 119, no. 7, 4573–4592, 2014.
8. R. H. Tyler, S. Maus, and H. Lühr, Satellite observations of magnetic fields due to ocean tidal flow. *Science*, vol. 299, no. 5604, 239–241, 2003.
9. S. Maus and A. Kuvshinov, Ocean tidal signals in observatory and satellite magnetic measurements. *Geophysical Research Letters*, vol. 31, no. 15, 2004.
10. A. Kuvshinov, 3-D global induction in the oceans and solid earth: recent progress in modeling magnetic and electric fields from sources of magnetospheric, ionospheric and oceanic origin. *Surveys in Geophysics*, vol. 29, no. 2, 139–186, 2008.
11. A. D. Chave and D. S. Luther, Low-frequency, motionally induced electromagnetic fields in the ocean. 1. Theory.. *Journal of Geophysical Research*, vol. 95, 7185–7200, 1990.
12. R. H. Tyler, L. A. Mysak, and J. M. Oberhuber, Electromagnetic fields generated by a three dimensional global ocean circulation. *Journal of Geophysical Research*, vol. 102, no. C3, 5531–5551, 1997.
13. N. Schnepf, A. Kuvshinov, and T. Sabaka, Can we probe the conductivity of the lithosphere and upper mantle using satellite tidal magnetic signals?. *Geophysical Research Letters*, vol. 42, no. 9, 3233–3239, 2015.
14. A. D. Chave, On the theory of electromagnetic induction in the earth by ocean currents. *Journal of Geophysical Research*, vol. 88, no. B4, 3531–3542, 1983.
15. A. Kuvshinov, A. Junge, and H. Utada, 3-D modelling the electric field due to ocean tidal flow and comparison with observations. *Geophysical Research Letters*, vol. 33, no. 6, 2006.
16. C. Manoj, A. Kuvshinov, S. Maus, and H. Lühr, Ocean circulation generated magnetic signals. *Earth, Planets and Space*, vol. 58, no. 4, 429–437, 2006.
17. M. Cheney, D. Isaacson, and J. C. Newell, Electrical impedance tomography. *SIAM review*, vol. 41, no. 1, 85–101, 1999.
18. E. Fainberg, A. Kuvshinov, and B. S. Singer, Electromagnetic induction in a spherical Earth with non-uniform oceans and continents in electric contact with the underlying medium - II. Bimodal global geomagnetic sounding of the lithosphere. *Geophysical Journal International*, vol. 102, no. 2, 283–286, 1990.

19. T. J. Sabaka, N. Olsen, R. H. Tyler, and A. Kuvshinov, CM5, a pre-Swarm comprehensive geomagnetic field model derived from over 12 yr of CHAMP, Ørsted, SAC-C and observatory data. *Geophysical Journal International*, vol. 200, no. 3, 1596–1626, 2015.
20. H. Kawakatsu, P. Kumar, Y. Takei, M. Shinohara, T. Kanazawa, E. Araki, and K. Suyehiro, Seismic evidence for sharp lithosphere-asthenosphere boundaries of oceanic plates. *Science*, vol. 324, no. 5926, 499–502, 2009.
21. C. A. Rychert and P. M. Shearer, A global view of the lithosphere-asthenosphere boundary. *Science*, vol. 324, no. 5926, 495–498, 2009.
22. E. Sarafian, R. Evans, J. A. Collins, J. Elsenbeck, G. A. Gaetani, J. B. Gaherty, G. Hirth, D. Lizarralde, et al., The electrical structure of the central Pacific upper mantle constrained by the NoMelt experiment. *Geochemistry, Geophysics, Geosystems*, vol. 16, no. 4, 1115–1132, 2015.
23. A. Chulliat, S. Macmillan, P. Alken, C. Beggan, M. Nair, B. Hamilton, A. Woods, V. Ridley, S. Maus, and A. Thomson, The US/UK World Magnetic Model for 2015–2020. 2015. NOAA Technical Report.
24. D. Stammer, R. Ray, O. B. Andersen, B. Arbic, W. Bosch, L. Carrère, Y. Cheng, D. Chinn, B. Dushaw, G. Egbert, et al., Accuracy assessment of global barotropic ocean tide models. *Reviews of Geophysics*, vol. 52, no. 3, 243–282, 2014.
25. N. Fofonoff, Physical properties of seawater: A new salinity scale and equation of state for seawater. *Journal of Geophysical Research: Oceans*, vol. 90, no. C2, 3332–3342, 1985.
26. T. Yoshino, T. Matsuzaki, S. Yamashita, and T. Katsura, Hydrous olivine unable to account for conductivity anomaly at the top of the asthenosphere. *Nature*, vol. 443, no. 7114, 973–976, 2006.
27. D. Wang, M. Mookherjee, Y. Xu, and S.-i. Karato, The effect of water on the electrical conductivity of olivine. *Nature*, vol. 443, no. 7114, 977–980, 2006.
28. K. M. Fischer, H. A. Ford, D. L. Abt, and C. A. Rychert, The lithosphere-asthenosphere boundary. *Annual Review of Earth and Planetary Sciences*, vol. 38, 551–575, 2010.
29. T. J. Sabaka, R. H. Tyler, and N. Olsen, Extracting ocean-generated tidal magnetic signals from swarm data through satellite gradiometry. *Geophysical Research Letters*, vol. 43, no. 7, 3237–3245, 2016.
30. A. Kelbert, A. Schultz, and G. Egbert, Global electromagnetic induction constraints on transition-zone water content variations. *Nature*, vol. 460, no. 7258, 1003–1006, 2009.
31. A. Semenov and A. Kuvshinov, Global 3-D imaging of mantle conductivity based on inversion of observatory C-responses-II. Data analysis and results. *Geophysical Journal International*, vol. 191, no. 3, 965–992, 2012.
32. R. H. Tyler, Strong ocean tidal flow and heating on moons of the outer planets. *Nature*, vol. 456, no. 7223, 770–772, 2008.
33. J. Saur, F. M. Neubauer, and K.-H. Glassmeier, Induced magnetic fields in solar system bodies. *Space Science Reviews*, vol. 152, no. 1–4, 391–421, 2010.
34. K. K. Khurana, M. G. Kivelson, K. P. Hand, and C. T. Russell, Electromagnetic induction from Europa's ocean and the deep interior. *Europa, The Univ. of Arizona Space Sci. Ser.*, p. 571, 2009.

35. A. V. Grayver and A. V. Kuvshinov, Exploring equivalence domain in non-linear inverse problems using Covariance Matrix Adaption Evolution Strategy (CMAES) and random sampling. *Geophysical Journal International*, vol. 205, 971–987, 2016.
36. N. Hansen and A. Ostermeier, Completely derandomized self-adaptation in evolution strategies. *Evolutionary computation*, vol. 9, no. 2, 159–195, 2001.
37. P. M. Saunders, Practical conversion of pressure to depth. *Journal of Physical Oceanography*, vol. 11, no. 4, 573–574, 1981.

Acknowledgments

Funding: This work is supported by the European Space Agency STSE Swarm + Innovation program (ESTEC contract No. 4000113885/15/NL/MP).

Author contributions: A.V.G. conducted the data inversion and analyzed the results; A.V.K. provided 3D forward modeling code; T.J.S. and N.O. processed and prepared satellite data; N.R.S. prepared extraneous electric current maps; N.R.S. and C.M. compiled depth-averaged seawater conductivity map. A.V.G., A.V.K. and N.R.S. designed the study and A.V.G. drafted the manuscript. All authors discussed the results and commented on the manuscript.

Competing interests: The authors declare that they have no competing interests.

Data and materials availability: All data needed to evaluate the conclusions in the paper are present in the paper and/or the Supplementary Materials. Additional data related to this paper may be requested from the authors.

Figures and Tables

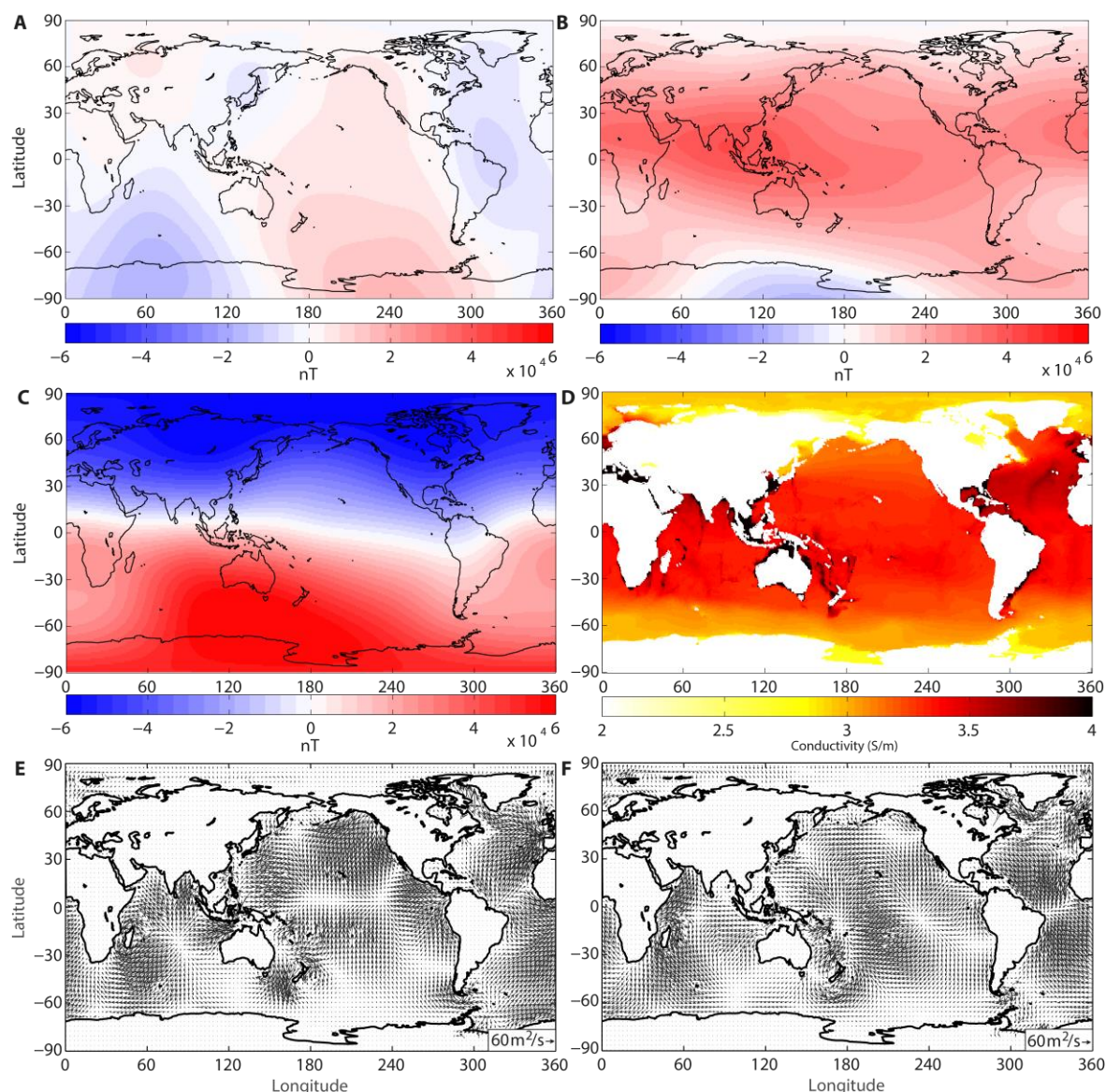


Fig. 1. Input used to derive the extraneous electric current due to tidal flow (cf. eq. 2). (A, B, C) Eastward, southward and upward components of the Earth's main (core) magnetic field for epoch 2010 (23). (D) Depth-averaged ocean water conductivity calculated for the year 2009 using global data of ocean salinity, temperature and pressure. (E, F) In-phase and quadrature parts of the depth-integrated horizontal water velocity of M_2 tide (7). Note the scale in the right bottom corner.

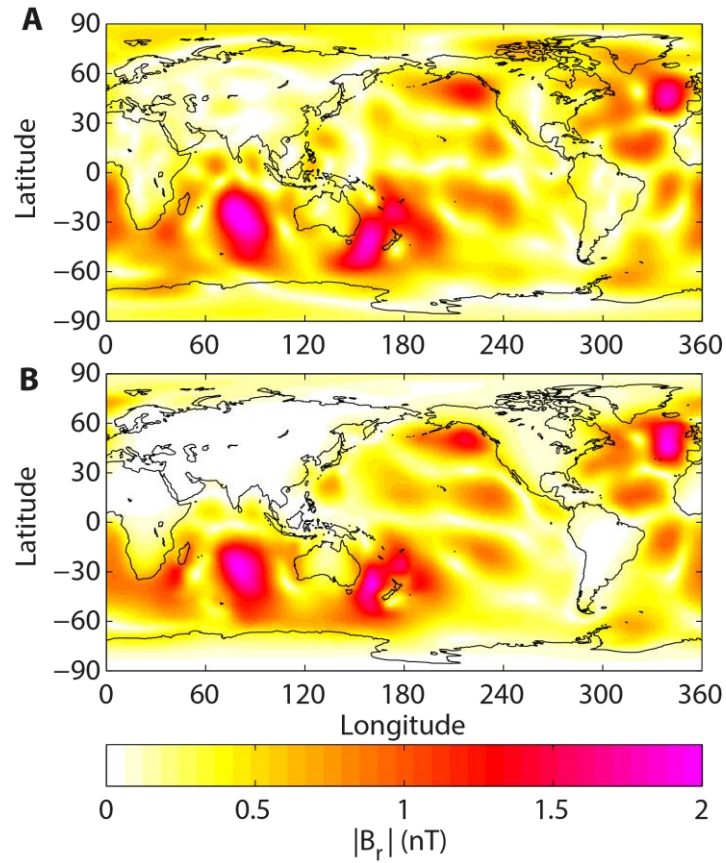


Fig. 2. Amplitudes of the radial magnetic field components due to the M2 tide at the altitude of 430 km. (A) Extracted from satellite data. (B) Calculated based on the recovered conductivity model.

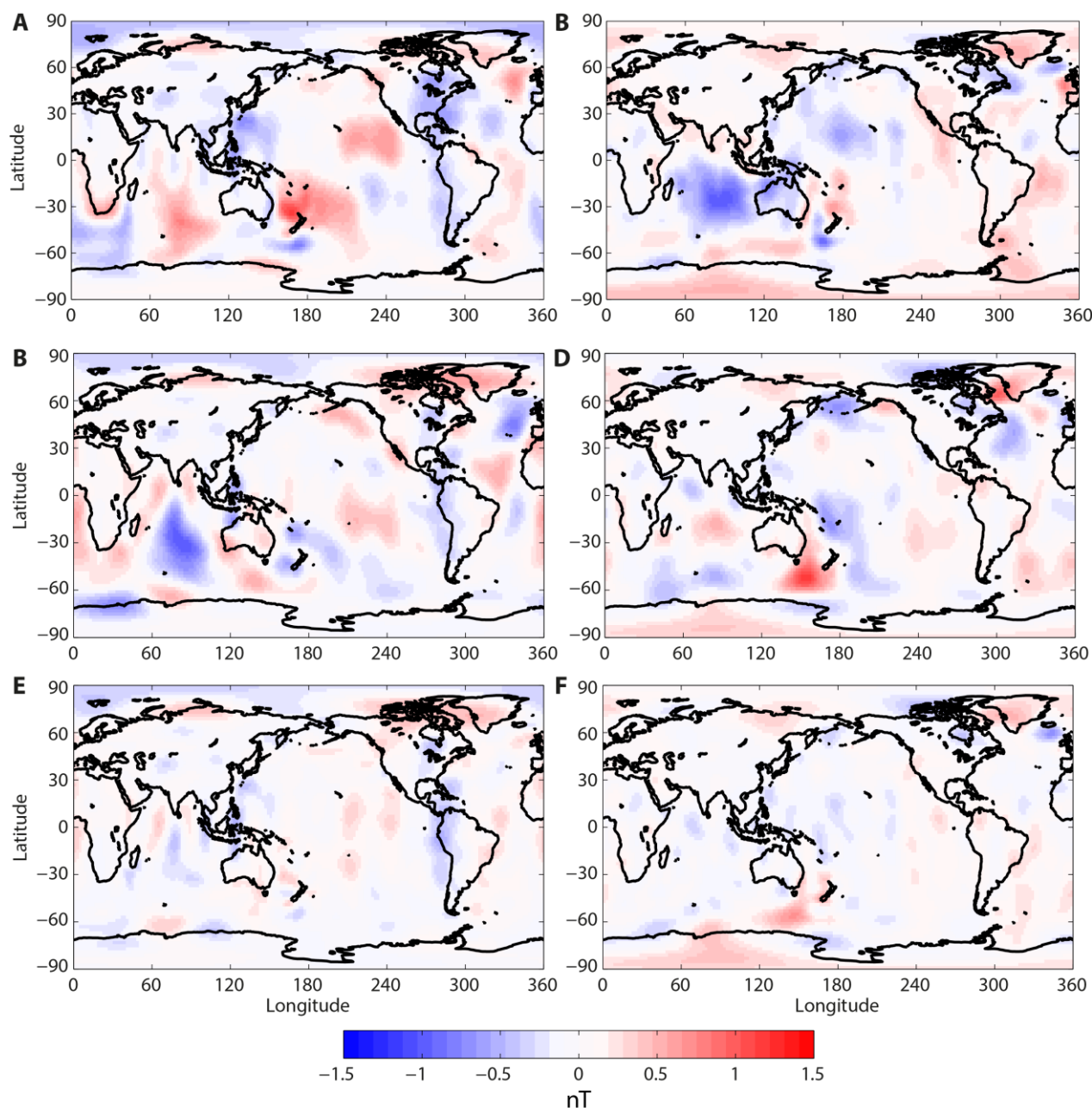


Fig. 3. Difference between observed and predicted in-phase (left) and quadrature (right) radial magnetic field components due to the tidal flow at the satellite altitude (430 km). (A, B) For an insulating mantle. (C, D) For a homogeneous mantle of 0.2 S/m conductivity (used as an initial guess for the inversion). (E, F) For the final model shown in Figure 4.

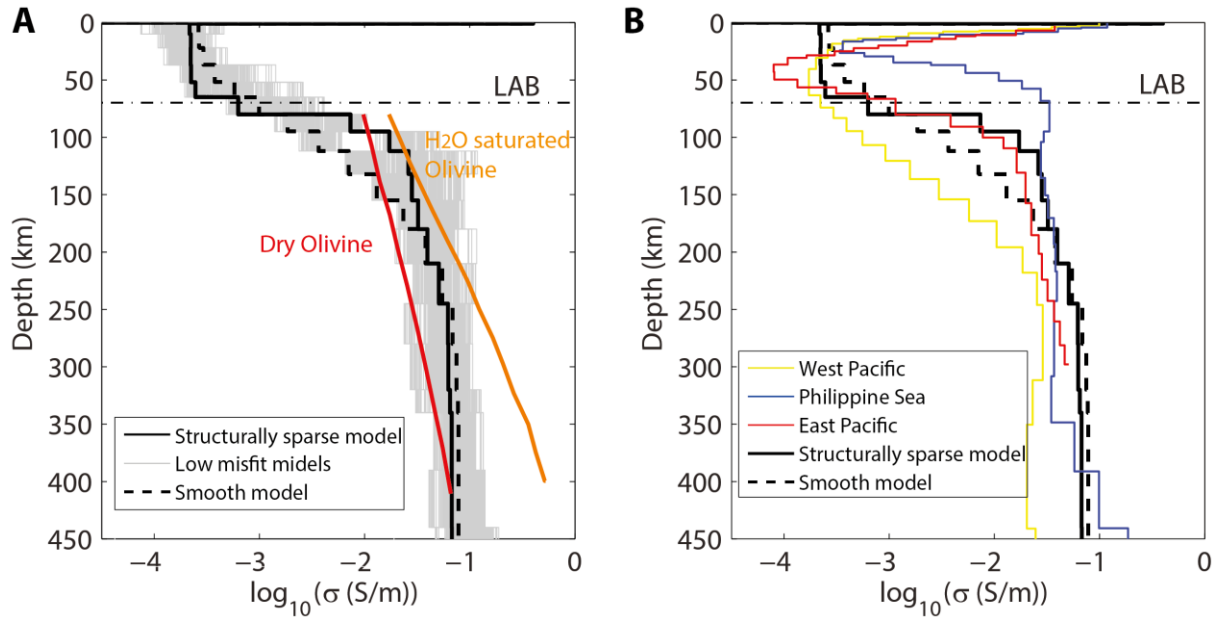


Fig. 4. The recovered global radial electrical conductivity models compared with mineral physics constraints and local models derived from seafloor magnetotelluric data. (A) Black solid and dashed lines, respectively, represent the most probable models obtained by using structurally sparse (that is, permit conductivity jumps, but allow as few features as possible) and smooth constraints in the inversion algorithm (35). The gray lines denote the 1000 models for which misfit differs no more than 10% from the most probable solutions. Conductivities of the dry and water-saturated olivine (1) are shown with red and orange lines, respectively. (B) The blue line represents the conductivity model from the Philippine Sea plate (< 60 Ma) (4), whereas the red curve represents that from the East Pacific region (70 Ma) (22) and the yellow line shows that from the West Pacific region (125-150 Ma) (4). The horizontal dash-dotted line marks the average oceanic LAB depth estimated from seismic data (21).

Supplementary Materials

Movie M1. Animation of the observed and predicted satellite magnetic tidal signals for the Earth's principal lunar semi-diurnal tide.

Data file S1. A 1x1 degree map of depth-averaged ocean electric conductivity produced following the method of (25). The salinity and temperature data used are from NOAA's 2009 World Ocean Atlas annual climatology, whereas local pressure was estimated using the method of (37).